

## An offshore Gabon full-waveform inversion case study

Bingmu Xiao<sup>1</sup>, Nadezhda Kotova<sup>1</sup>, Samuel Bretherton<sup>1</sup>, Andrew Ratcliffe<sup>1</sup>, Gregor Duval<sup>1</sup>, Chris Page<sup>1</sup>, and Owen Pape<sup>1</sup>

### Abstract

Velocity model building is one of the most difficult aspects of the seismic processing sequence. But it is also one of the most important: an accurate earth model allows an accurate migrated image to be formed, which allows the geologist a better chance at an accurate interpretation of the area. In addition, the velocity model itself can provide complementary information about the geology and geophysics of the region. Full-waveform inversion (FWI) is a popular, high-end velocity model-building tool that can generate high-resolution earth models, especially in regions of the model probed by the transmitted (diving wave) arrivals on the recorded seismic data. The history of the South Gabon Basin is complex, leading to a rich geologic picture today and a very challenging velocity model-building process. We have developed a case study from the offshore Gabon area showing that FWI is able to help with the model-building process, and the resulting velocity model reveals features that improve the migrated image. The application of FWI is made on an extremely large area covering approximately 25,000 km<sup>2</sup>, demonstrating that FWI can be applied to this magnitude of survey in a timely manner. In addition, the detail in the FWI velocity model aids the geologic interpretation by highlighting, among other things, the location of shallow gas pockets, buried channels, and carbonate rafts. The concept of actively using the FWI-derived velocity model to aid the interpretation in areas of complex geology, and/or to identify potential geohazards to avoid in an exploration context, is applicable to many parts of the world.

### Introduction

Full-waveform inversion (FWI) offers the potential to replace the conventional imaging step in seismic processing with an inversion for the specific geophysical, or even geological, earth parameter of interest. It does this by attempting to model all of the events in the recorded data — clearly an ambitious target. Although this ultimate objective is still probably many years away due to various computational and technical challenges in FWI that are still to be overcome, this topic is at present hugely popular in the oil exploration community in academia and industry. This has been the case for a number of years since it gained significant momentum in the late 2000s following the publication of some impressive field examples as computing power caught up with algorithmic complexity. The current paradigm in industrial applications is to use FWI to solve velocity complexity in the areas that are well-probed by the diving or transmitted waves and derive a velocity model that gives uplift in the final migration. This work generally follows this paradigm but with two extra elements: (1) we use the FWI-derived velocity model to aid and offer additional context to the geologic interpretation

of the seismic image and (2) FWI is applied to an extremely large data set.

The concept of FWI originated more than 30 years ago with the works of Lailly (1983) and Tarantola (1984). It was significantly ahead of its time with regard to what could be achieved with the computing power of the day, meaning even small-scale industrial applications in 3D were beyond its reach. It survived as an active research topic in academia through the 1990s, particularly with the frequency-domain approach of Pratt (1999) that concentrated specifically on the first arrival, diving wave energy. Work on the technique evolved throughout the 2000s, resulting in some stand-out field-data applications shown in Plessix (2009) and Sirgue et al. (2009) among others. Most industrial work since then has been to establish the robustness of the technique, while extending the applicability of the method with improved technology and improved data acquisition. Indeed, in a good acquisition geometry for FWI, recording longer offsets and lower frequencies are the main drivers to give a deeper penetration depth of the diving waves and to help alleviate cycle-skipping problems between the real and modeled synthetic shot gathers (Virieux and Operto, 2009).

<sup>1</sup>CGG, Crawley, UK. E-mail: bingmu.xiao@cgg.com; nadezhda.kotova@cgg.com; samuel.bretherton@cgg.com; andrew.ratcliffe@cgg.com; gregor.duval@cgg.com; chris.page@cgg.com; owen.pape@cgg.com.

Manuscript received by the Editor 29 February 2016; revised manuscript received 8 July 2016; published online 13 October 2016. This paper appears in *Interpretation*, Vol. 4, No. 4 (November 2016); p. SU25–SU39, 12 FIGS.

<http://dx.doi.org/10.1190/INT-2016-0037.1>. © 2016 Society of Exploration Geophysicists and American Association of Petroleum Geologists. All rights reserved.

In this paper, we use a data set from offshore Gabon that was acquired with a broadband, long-offset streamer profile. We start by outlining the geologic setting of the data set before describing the details of the survey acquisition. The next two sections highlight our FWI methodology and show the FWI results, imaging uplift, and some of the quality control (QC) checks that we do. We then use the resulting seismic image and the FWI-derived velocity model to offer some interpretation of the area, with a particular emphasis on the complexities in the velocity model arising from the geologic history. We discuss some perspectives on extending the project before concluding. The objective of this work is to show the potentially exciting step of using information in the velocity model to aid the geologic interpretation and the

exploration and production development, such as identifying shallow geohazards to avoid when drilling, as well as highlight the very large areas that can now be tackled with FWI.

### Geologic setting

In the West Africa Atlantic Margin, one of the last underexplored regions is the deepwater area of the South Gabon Basin. Successful exploration in the conjugate South Atlantic Margin offshore Brazil has sparked renewed interest in deepwater presalt plays in the whole offshore southwestern region of Africa, including Gabon, with significant discoveries offshore Angola and Congo, the latter being geographically close to the current survey. Figure 1 shows a generalized stratigraphic column of the area, which shows how the South Gabon Basin developed in three main stages: prerift, syn-rift, and postrift. Figure 2a and 2b highlights these stages on a regional geologic cross section and regional seismic line, respectively. In terms of hydrocarbon prospectivity, exploration targets include the deep, high porosity, high permeability, subsalt Barremian to Aptian sandstones; the suprasalt Albian-age Madiela carbonate turtlebacks; and the Cretaceous Tertiary turbidite sands that provide established targets further south offshore Angola and Congo. The diversity of these reservoir types, and the broad depth range at which they are found, means that an accurate velocity model is needed to image these heterogeneities at all levels of the geologic section. In terms of structural complexity, the presalt section offers potential traps formed by tilted fault blocks and broad rollover anticlines that are sealed by Aptian claystones or salt. We note that in the case of the South Gabon Basin, these structures need to be imaged at great depth below the Aptian salt layer. In the postsalt section, traps comprise drapes over salt domes and structural/stratigraphic traps of sand-rich channels within turbidite systems that are sealed by marine mudstones. In this case, we highlight again the necessity of an accurate velocity model in support of high-resolution broadband seismic to resolve these thin reservoir beds and stratigraphic pinch-out traps. Of the six wells that have been drilled in our 3D survey area, only one of them penetrated into the presalt level, leaving the deeper prospectivity in the survey area still an unanswered question. Finally, we note that our terminology for “salt” in this paper is to describe any fast velocity, often

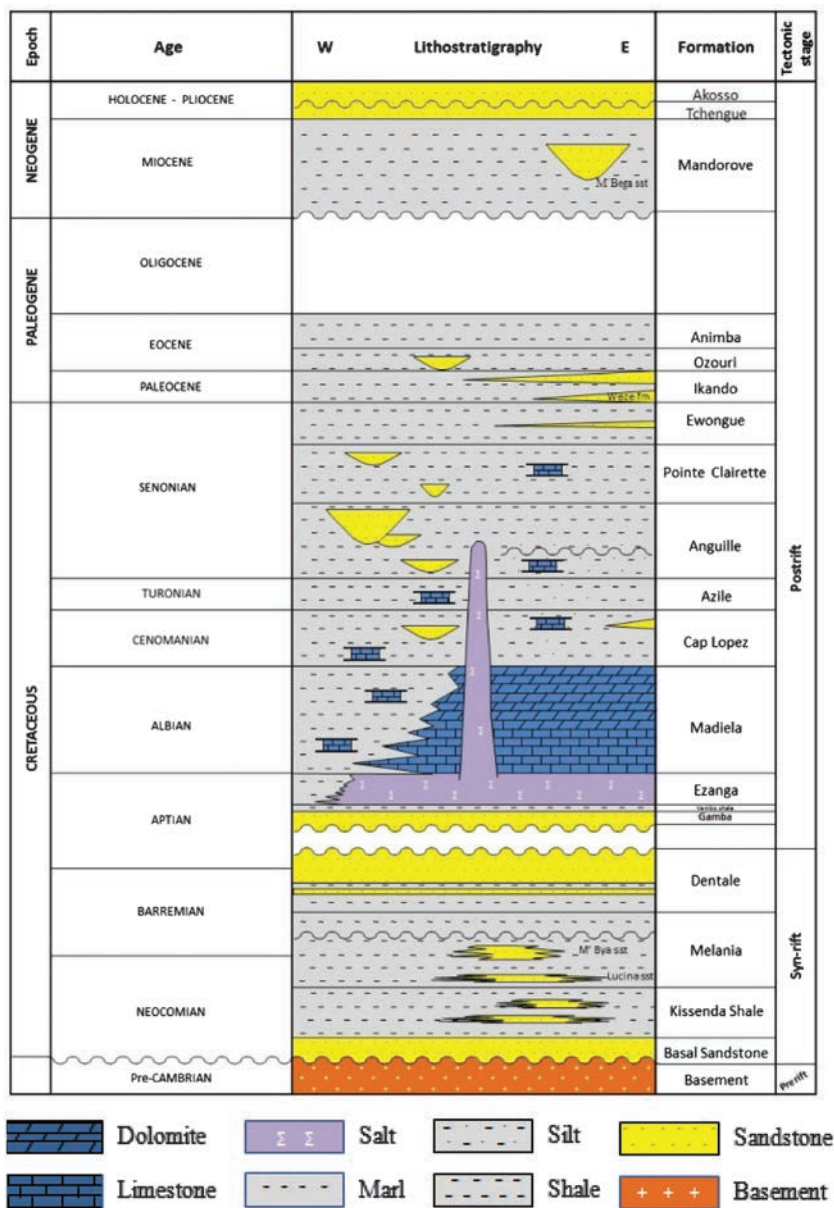


**Figure 1.** Generalized stratigraphic column of the South Gabon basin, with the three main rift stages highlighted.



deformed, evaporite layer, rather than the sodium chloride mineral, favoring the geophysicists' generic definition rather than the geologists' specific one.

### Survey details

The preliminary aspects of this project, including survey design and acquisition, are discussed in more detail in [Duval and Firth \(2015\)](#). Here, we highlight the main aspects of the survey location, size, and acquisition configuration that are relevant to this work.

### Location and size

This data set was acquired offshore Gabon between 2014 and 2015. Figure 3 plots an aerial map of the region. The area of acquisition is just more than 25,000 km<sup>2</sup>, covering 11 blocks, some of which are part of the latest licensing round for the Gabonese Republic's Ministry of Petroleum and Hydrocarbons. The survey area is a very large number for an FWI project. The water depth varies from approximately 100 m in the northeast nearer to the Gabon coastline, down to approximately 3.5 km in the deepwater area in the southwest. To aid the reader, we try to put the size of this area into perspective in two ways: first, we recall the seminal ocean-bottom seismic-derived FWI results, that sparked massive industry interest in the late 2000s, being of order approximately 100–200 km<sup>2</sup>: the industry has clearly come a long way in the past six or seven years. Second, in Figure 3, we

show a map of the UK on the same scale and overlaid with the outline of the survey. As can be seen, this survey would cover the entire southeastern corner of the UK, a truly massive area.

### Acquisition configuration

The survey was acquired with a variable-depth streamer configuration designed to provide broader bandwidth seismic data ([Soubaras and Dowle, 2010](#)). This is achieved by a combination of the use of solid streamers that have a reduced recording noise level compared with gel streamers, along with a variable-depth streamer profile that offers benefits for preserving frequencies that would normally be attenuated by the sea-surface ghost effect ([Soubaras, 2010](#)). In particular for FWI, having the deepest tow at the longest offsets offers the double benefit of reduced ghost-notch attenuation and a quieter recording environment. This generates higher-quality lower-frequency seismic data at the longest offsets that are the most useful to drive FWI ([Jupp et al., 2012](#)). There are two shooting vessels involved in the acquisition, each towing 10 streamers that are 10 km long, with 600 m between each sail line. The nominal shot spacing is 25 m in a flip-flop manner, whereas the cables are 120 m apart with receivers every 12.5 m and a near offset of 165 m. A ray-traced analysis of the diving waves through the starting velocity model of the area for the southwest and northeast shooting

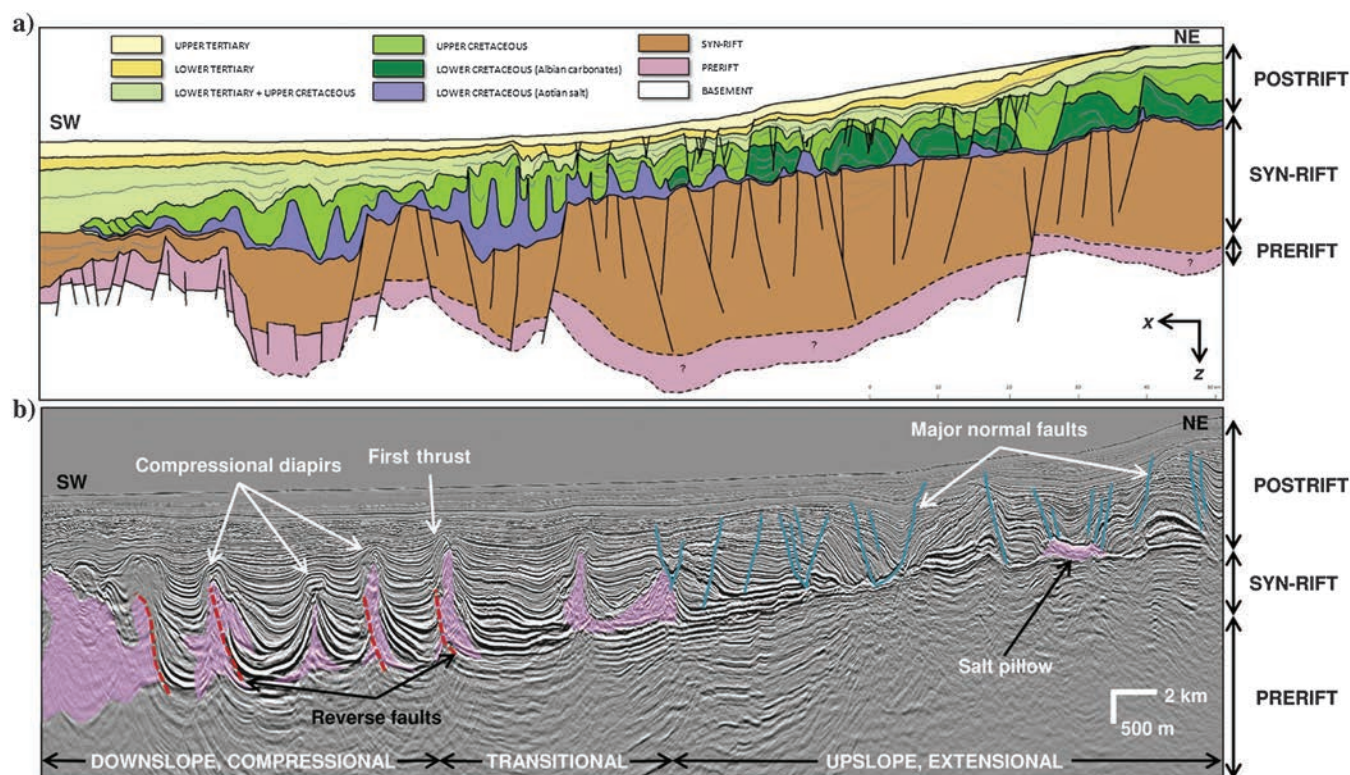


**Figure 2.** (a) Regional geologic cross section and (b) regional seismic line, with the northeast direction to the right and the southwest to the left. Illustration of the three deformation domains seen in the offshore Gabon data set: compressional in the southwestern, downslope region on the left; transitional in the center; and extensional in the northeastern, upslope region on the right.

directions is shown in Figure 4 for three typical locations in the survey. These displays show that the maximum offset of 10 km gave good diving wave coverage down to the salt/carbonate level, whereas it is observed that significantly larger offsets are needed to get penetration through these high-velocity structures.

### FWI methodology

A standard FWI algorithm is based on minimizing a cost function  $J$  representing the mismatch between real and modeled synthetic data that have been generated from the current earth model using the two-way wave equation (Lailly, 1983; Tarantola, 1984; Pratt, 1999). This minimization is typically done by forming a gradient in this cost function through the use of the adjoint-state method (Plessix, 2006) and then either using a steepest descent or Newton/Gauss-Newton optimization algorithm. The choice of this type of local optimization algorithm, as opposed to a global algorithm, is purely dictated by the computation cost of a problem with such a large number of unknowns. In the example we will present here, the final velocity model contains approximately 1.85 billion grid cells; i.e., we are trying to solve a 1.85 billion-dimensional problem. Far and away the most common form of mismatch measurement is the straightforward least-squares difference between real and modeled synthetic data, generally with an appropriate normalization factor between the data sets:

$$J(\mathbf{m}) = \frac{1}{2} \sum_{j=1}^M [\mathbf{u}_j(\mathbf{m}) - w_j \mathbf{d}_j]^T \mathbf{W}_j^T \mathbf{W}_j [\mathbf{u}_j(\mathbf{m}) - w_j \mathbf{d}_j], \quad (1)$$

where  $\mathbf{m}$  is the earth model vector,  $j$  is the summation index over all shot-receiver pairs  $M$  in the survey,  $\mathbf{u}$  and  $\mathbf{d}$  are the synthetic modeled and observed real data traces, respectively, for each of these pairs,  $\mathbf{W}$  is a data weight function,  $w$  is a trace normalization factor, and the superscript  $T$  corresponds to the matrix transpose operation. For a complete description of FWI, with full historical context and references, we refer the interested reader to the paper by Virieux and Operto (2009).

### Wavelet estimation

Given that a direct difference between the real and modeled synthetic data drives most FWI algorithms, the accuracy of the source wavelet that generates the synthetic data is a key aspect for the success of FWI. A variety of methods can be used to estimate it, such as automatically as part of the FWI process (Pratt, 1999; Rickett, 2013), from an inversion of the direct arrival in deeper water settings (Davison and Poole, 2015), from a modeled gun signature (Jupp et al., 2012) or via direct or indirect extraction from the field data themselves. When the required data exist, our preferred method is from inversion of near-field hydrophone (NFH) measurements to provide a wavelet free from any ghosts (Ziolkowski et al., 1982; Ni et al., 2014).

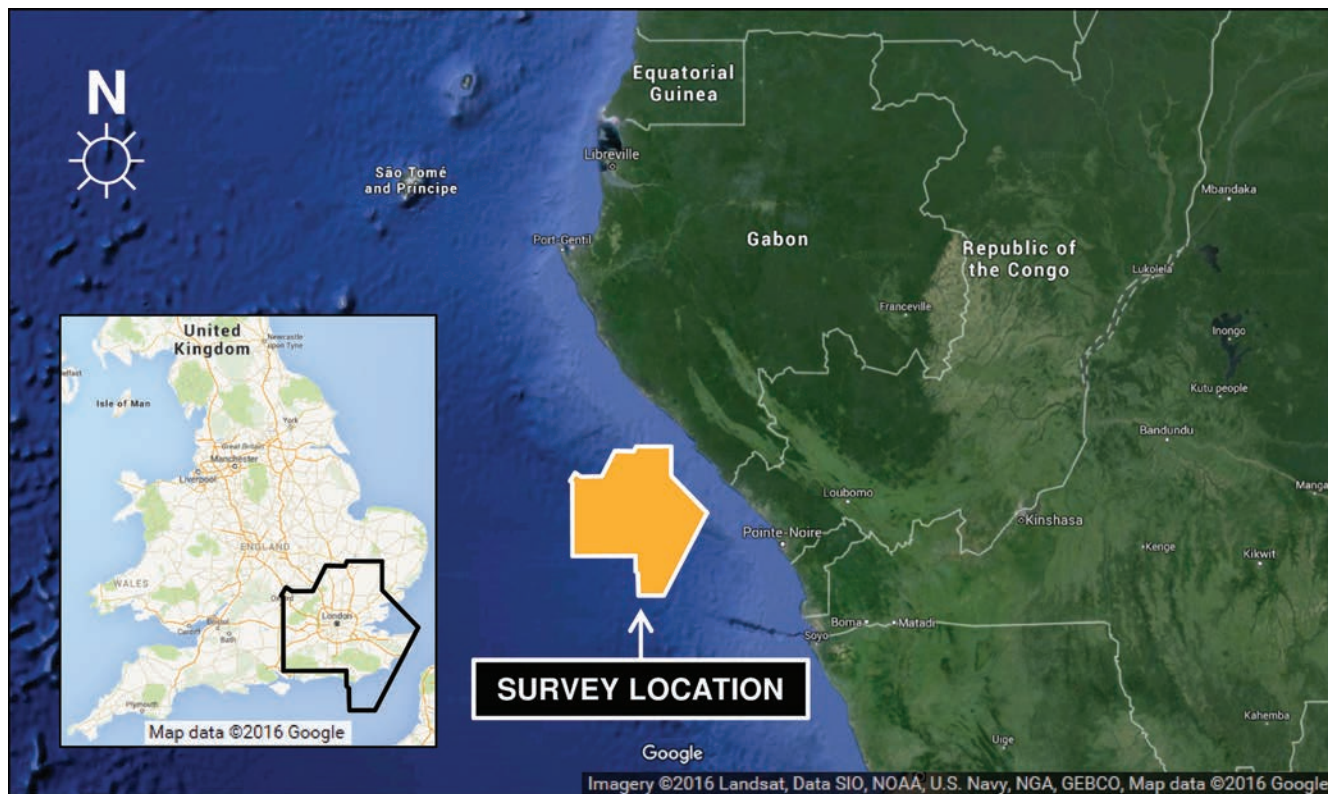


**Figure 3.** Aerial map of the survey location offshore Gabon. For reference, we also plot a map of the UK on the same scale to highlight the size of the survey.



The NFH data were recorded in this survey and, hence, we use this method here.

### Data preprocessing

We do not deghost or demultiple the field data and instead rely on injecting a ghost-free wavelet into a forward-modeling process, with a free surface, to generate the synthetic data (Ratcliffe et al., 2011). In a high-frequency imaging process, such a choice of leaving the free-surface effects in the data would almost certainly lead to crosstalk artifacts in the image caused by spurious correlations between primaries and multiples (see, e.g., Wang et al., 2014a). However, in the context of FWI, which is an iterative inversion process, this seems not to be the case and FWI appears to self-correct crosstalk artifacts from one iteration to the next (Wang et al., 2014b). Although beyond the scope of this paper, we believe this topic is an interesting one that needs a greater theoretical understanding by the geophysical community, for example, Chauris and Plessix (2013) and Sun and Symes (2012) discuss this for a similar inversion problem. This workflow has the benefit of making the preprocessing for FWI a fairly simple procedure, free from the often complicated and time consuming demultiple and deghosting processes. First, we apply a very low-cut filter to attenuate noise below 2 Hz, followed by a high-cut filter to 15 Hz with appropriate resampling for more efficient storage of the data set for FWI. Although the application of this high-cut filter clearly limits the maximum frequency we can run FWI to, it is not a specific limitation for the work we present here and we can revisit this step if higher-frequency FWI is required. We then perform basic trace edits, swell noise attenuation, and an outer and inner mute to highlight the diving waves on the shot record.

### Velocity update

We use a time-domain FWI algorithm, published in detail in Warner et al. (2013) and subsequently updated by Ratcliffe et al. (2014) that is based on the acoustic wave equation and finite-difference scheme described in Zhang et al. (2011):

$$\frac{1}{v_0^2} \frac{\partial^2}{\partial t^2} \begin{pmatrix} p \\ r \end{pmatrix} = \begin{pmatrix} 1 + 2\varepsilon & \sqrt{1 + 2\delta} \\ \sqrt{1 + 2\delta} & 1 \end{pmatrix} \times \begin{pmatrix} \frac{\partial^2}{\partial x^2} + \frac{\partial^2}{\partial y^2} & 0 \\ 0 & \frac{\partial^2}{\partial z^2} \end{pmatrix} \begin{pmatrix} p \\ r \end{pmatrix}, \quad (2)$$

where  $v_0$  is the velocity,  $p$  is the horizontal stress,  $r$  is the vertical stress, whereas

$\varepsilon$  and  $\delta$  are the dimensionless anisotropy parameters of Thomsen (1986). The wave equation presented here has vertical transverse isotropic anisotropy, but can be extended to tilted transverse isotropic (TTI) anisotropy with an appropriate replacement of the spatial differential operators (e.g., see equation 21 in Zhang et al., 2011). Density can be introduced into this wave equation in the standard manner and is used in this work. The inversion scheme itself is an iterative update to the P-wave velocity via a linearized least-squares process, using the multi-scale, increasing frequency band, approach of Bunks et al. (1995). In addition, we highlight that the inversion results presented here do not have any regularization terms in the cost function of equation 1. Because we use a time-domain algorithm, whenever we quote a frequency for FWI in this paper, we actually refer to the high-cut frequency of a low-pass filter, rather than a

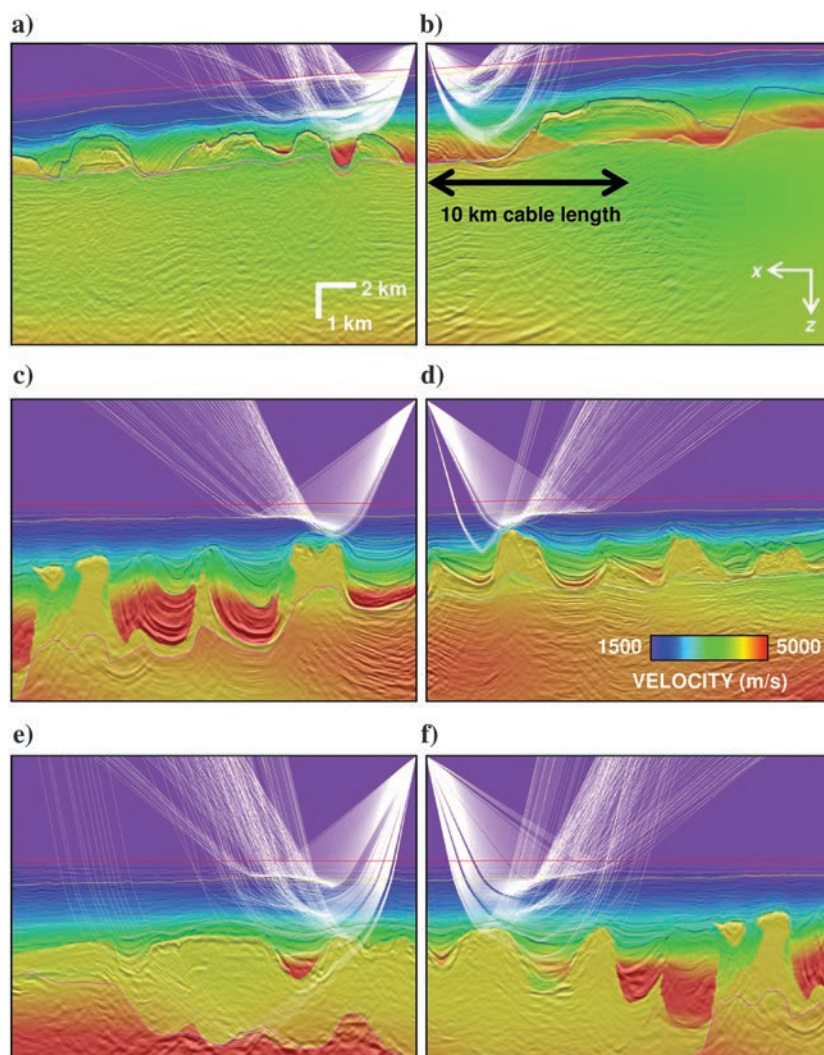


**Figure 4.** Example of a ray-traced diving wave analysis in a shallow-water, carbonate-dominated, area for: (a) southwest and (b) northeast shooting directions, respectively. Similar analysis is shown in (c) and (d) for a more central, salt-dominated, area, whereas (e) and (f) show a deepwater area from the southwest of the survey. These displays show that the recorded diving waves in the 10 km streamer penetrate down to the top-salt/carbonate level.

single frequency. Including reflections and transmitted wave energy can be beneficial to FWI in the regions that are well-probed by the diving waves (Warner et al., 2013). At depths below the level of the diving wave penetration, the updates are driven only by reflections. The validity of these perturbations assumes an accurate macro velocity model at this depth, which varies from project to project, and an appropriate density behavior. In this study, we assume a Gardner et al.'s (1974) law relationship between density and P-wave velocity, with a smoothly varying modification for water density. Very nice results are obtained when these assumptions are valid (see, e.g., Kumar et al., 2014). In this project, we acknowledge that uncertainties still exist in the deeper velocity model and, hence, we only use the FWI update down to the level of the diving wave penetration, effectively the top salt. Overall, this algorithm and methodology has proved itself on many field data sets with different acquisition types and geometries involving geologies from all around the world.

The starting velocity model comes from the current stage of a larger velocity model-building process down to basement level. Here, FWI is being used as an active component within this larger model build, rather than at the end of the process as is often seen. At present, this model has been built down to the salt level and contains TTI anisotropy that is necessary for the complexity of the region, being derived from a nonlinear slope tomography process (Guillaume et al., 2008). This also included an update of Thomsen's (1986) epsilon parameter in the tomography. Well calibration is not possible because only very limited well data are available in this region. Hence, delta is scaled on a layer-by-layer basis according to the average epsilon in the layer. The starting frequency for FWI was chosen to be 4 Hz by checking the data quality at this frequency and confirming that cycle skipping was not observed between the real and modeled synthetic data at this frequency (see the later subsection on QC). The application here of the classical diving-wave-driven FWI using the least-squares data difference needs the underlying kinematics of the starting velocity model to be accurate to within half a cycle (see, e.g., Virieux and Operto, 2009). The fact that the data were not observed to be cycle skipped indicates that these kinematics are accurate enough to start the inversion. The question of the maximum frequency in the FWI is generally a compromise between the observed improvements in the results as we push to higher frequency and the resulting computational cost of obtaining those results. Given the extremely large area that we are updating, a value of 8 Hz was chosen as a realistic number. This was based on results obtained from a test swath that balanced a good observed uplift in the velocity model with acceptable runtimes. The interval between adjacent frequencies was also tested on this swath ( $\Delta f = 1$  Hz versus  $\Delta f = 2$  Hz), and it was found the larger frequency step gave very similar results to the smaller one. Hence, the (high-cut) frequencies used in

production were 4, 6, and 8 Hz, with eight iterations per frequency band and a one-in-eight shot-skipping strategy per iteration, such shot skipping done on top of any initial shot decimation (see next section).

### Spatial sampling and acquisition footprint

Most geophysical textbooks discuss the question of an adequate spatial sampling interval of the wavefield using Nyquist-type arguments (see, e.g., Sheriff and Geldart, 1995). Ideally, these arguments hold for the shot- and receiver-side sampling in  $x$  and  $y$ , although on the shot side, it is often thought of as an illumination question, rather than an aliasing issue. Drawing from those works, we quote that a required spatial sampling interval for a plane-wave returning to the surface is

$$\Delta \leq \frac{v}{2f \sin \theta}, \quad (3)$$

where  $\Delta$  is the spatial sampling interval,  $v$  is the local velocity,  $f$  is the seismic frequency, and  $\theta$  is the angle of the wavefield with the vertical. In FWI, the cost is directly proportional to the number of shots used, whereas extra receivers within the existing maximum offset range are effectively computed for free and only contribute to the memory and hardware input/output. For typical FWI frequencies of  $<10$  Hz, the receiver side sampling in  $x$  and  $y$  is often satisfied by the raw acquisition sampling, even in the worst case scenario of a wave traveling horizontally. If not, then interpolation between the receivers rectifies the situation and adds minimal cost overall. However, on the shot side, we are used to observing a sail-line footprint in the velocity model related to the crossline, or  $y$ , sampling. This is especially true in the shallow due to the raw acquisition spacing between sail lines. Fixing this by interpolating shots between sail lines is possible, but with direct and significant cost implications in the FWI. In most cases, the sail-line footprint in the velocity model can be successfully attenuated either during or after FWI using a simple processing procedure, as described in Jones et al. (2013), and we apply this here as well. For the illumination related to the shot  $x$  sampling, in this data set, we are helped by the deepwater environment and, having obtained a good estimate of the water column velocity via other methods, we do not need to update it with FWI. This means that the shot sampling at the surface only needs to be good enough to sample energy returning to the surface at nonhorizontal incidence angles, which comes from below the water bottom. The deeper the water bottom, the closer toward vertical this incidence angle will be and, hence, the lower our sampling requirements. As an example of this, Figure 5 shows a comparison of the raw velocity perturbations from the deepest water area computed from initial shot  $x$  samplings of 400 and 800 m, prior to the one-in-eight shot skipping mentioned in the previous section. We see a clear artifact in the 800 m sampled data that disappears with a 400 m shot spacing. Given that there are



significant variations in the water depth throughout the survey region, we use a shot spacing of 200 m for the majority of the production work, again with such shot decimation done prior to the shot-skipping strategy mentioned in the previous section. Although this sampling is overkill in the deepest water areas, it does maintain a uniform illumination in the update, does not harm the results, and should increase the statistical stability of the update. However, as we enter the shallowest waters closest to the Gabon coastline, we need to reduce this shot sampling to 100 m to remove the sampling artifact.

### Salt and FWI

High-velocity contrasts across salt boundaries mean that salt bodies are not a natural partner with current FWI algorithms. This is in part due to the difficulty in getting the diving waves to penetrate very deep into the salt body itself. Also, combining such a large velocity contrast with the often extreme rugosity of the salt body shape causes extremely complex wavefields that are potentially even further complicated by elastic effects that are not modeled in acoustic FWI code. That said, a realistic goal should be to obtain a good update from FWI above the salt, and perhaps generate some information about the salt boundary itself. Wang et al. (2015) show that one element in obtaining the best possible sedimentary update above salt structures is to have an accurate top-salt boundary and propose an iterative scheme of FWI followed by top-salt picking, starting from a sedimentary-flood model. An accurate top-salt horizon pick throughout the entire survey was not available at the time the current FWI was run. Hence, we started this FWI from a sedimentary-flood velocity model and find that it produces a sensible perturbation that, as we will see later, leads to uplift in the image and adds to the geologic story. In essence, we have run the first pass of Wang et al.'s (2015) iterative scheme. In subsequent model-building phases, there are proposals to revisit the FWI starting from a model with an accurate top-salt pick, namely, the second pass of Wang et al.'s (2015) scheme.

### FWI and imaging results

In this section, we present the FWI and imaging results, but leave the main interpretational aspects and discussion to the next section. The size of the survey makes it difficult for the full-scale images to do justice to the results. Hence, we only show a handful of these types of images and rely on zooms of specific areas to see the detail. We have derived a complex model and at this stage of the project we use a controlled beam migration for QC of the imaging (Vinje et al., 2008). This has the benefit of being able to honor some of the complexity in the velocity model, with a faster turnaround that is appropriate for a QC process than, for example, reverse time migration. As we will mention in the section on "Suggestions for further study," the final imaging product will be generated with a reverse time migration process. Hence, our expectation is that any improvement seen in the QC images shown here will be, at the

very least, matched by the higher-end algorithm used in the final product.

### Velocity update

In Figure 6, we show the starting and FWI-updated velocity models for an inline through the southeasterly part of the survey, overlaid with an associated migrated image. The length of the line and large dynamic range of the color map needed to avoid saturation combine to make this comparison difficult. That said, we show these displays to allow the reader to extract two pieces of information: (1) to get some context of the regional behavior and complexity of the velocity model with reference to the seismic and (2) to indicate that the FWI update does not make step-changes to the background velocity model but instead alters the existing behavior, adding resolution as it goes. Figures 7 and 8 show example depth slices at 3500 and 3700 m, respectively, extracted from "small" areas of the whole volume for the starting and FWI updated velocity models, with migration overlays, as well as the migration only and the velocity perturbation only. We say "small," but it is worth remembering that the area in these displays is approximately 1000 km<sup>2</sup>, which itself is larger than most industrial FWI projects. These depth slices were chosen as being typical for the volume, where we see an increase in resolution and a number of interesting features coming through in the velocity model after FWI. For example, on these slices, we see channels containing high- and low-velocity infill material that are being very clearly picked out by FWI and, in general, are easier to see in the velocity model than in the seismic itself. Also, as mentioned before, below the top salt, the velocity models are not well-probed by diving waves and have been flooded with a salt velocity in those regions for these displays and the migrations.

Turning now to the imaging results, we first comment that, as mentioned earlier, success of FWI relies on the kinematics of the starting model being accurate enough, so as not to generate modeled data that are cycle skipped with respect to the real data. In this example, the kinematics come from a nonlinear slope

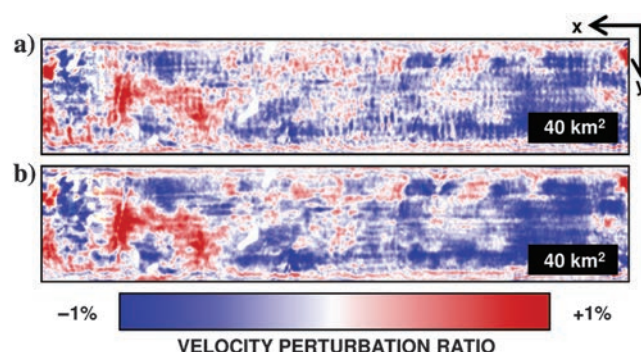


**Figure 5.** Depth slices at 3240 m of the FWI velocity perturbation for: (a) 800 m shot- $x$  spacing and (b) 400 m shot- $x$  spacing. The artifact related to spatial sampling disappears with the denser shot- $x$  spacing.

tomography process and are already very good, generating predominately flat gathers, as we will see. Hence, in comparison with the well-known published examples of extremely large gas clouds causing specific seismic obscured zones beneath the gas, with images that are healed by using the FWI velocity model (for example, [Sirgue et al., 2009](#)), we need to be realistic in our expectations for the uplift in the imaging here, where we have different geologic and different imaging challenges. That said, the extra resolution in the velocity model coming from the application of FWI will be of further benefit when we come to interpret the velocity model and seismic image. Figure 9 shows an example subset of common image gathers and the typical uplift in the gathers' flatness seen by migrating with the FWI updated velocity model. In Figure 10, we show a series of panels from various regions in the survey of migrated images before and after the FWI update, followed by the FWI-migrated image with the FWI velocity (after salt flood) and perturbations (before salt flood) overlaid. The improvements in imaging are sometimes subtle, such as correcting for small push-downs or pull-ups related to local velocity anomalies and sharpening of faults, and sometimes very clear, such as beneath some

of the salt diapirs or on the salt flanks. These types of changes after FWI almost always give rise to improvements in the imaging and are seen throughout the whole survey. In addition to the increase in resolution, especially at shallow-to-medium depths, a large number of the geologic features in the velocity model are now consistent with the migrated stack. Hence, we use Figure 10 to discuss the interpretational aspects of the velocity model in the section on "Geologic interpretation."

### Quality control

The FWI has potential pitfalls in its application and its success relies on asking a number of key questions before, during, and after the process (for more discussion, we refer the interested reader to [Warner et al. \[2013\]](#) and [Ratcliffe et al. \[2013\]](#)). For example, as already discussed, we must have confidence in: our pre-processing of the seismic data, our estimation of the wavelet, our modeling/inversion strategy, and what to expect from different acquisition geometries. As discussed earlier in this section, we also checked that the imaging improves after migration with the FWI velocity model. This leaves the primary remaining questions of choosing the starting frequency and obtaining an adequate starting velocity/anisotropy model. These questions are linked and can be expressed as making sure that the real and modeled synthetic data are not cycle skipped on the shot gathers, namely that they do not differ by more than half a cycle. This comparison can be done directly in the shot record domain, either by simply overlaying or toggling the displays. Figure 11 shows another way of displaying this information by interleaving blocks of real and synthetic data that have been filtered back to the starting FWI frequency of 4 Hz. In this display, Figure 11a and 11b shows the modeled data generated using the starting and FWI-updated velocity models, respectively. This enables us to have confidence that the starting model is adequate. This can be done for a handful of shots, but it is a time-consuming process and, clearly, looking at every shot is not a feasible QC strategy, even in the smallest of production surveys, let alone one such as this with more than 1.5 million shots. Hence, we use the strategy of initially looking at a very sparse sampling of shots in the data, then transferring across to the QC method of [Martinez-Sansigre and Ratcliffe \(2014\)](#) to check for cycle skipping over the whole survey, with a reality check of the QC compared with the shot gather displays. This QC attribute computes the time shift and dominant fre-

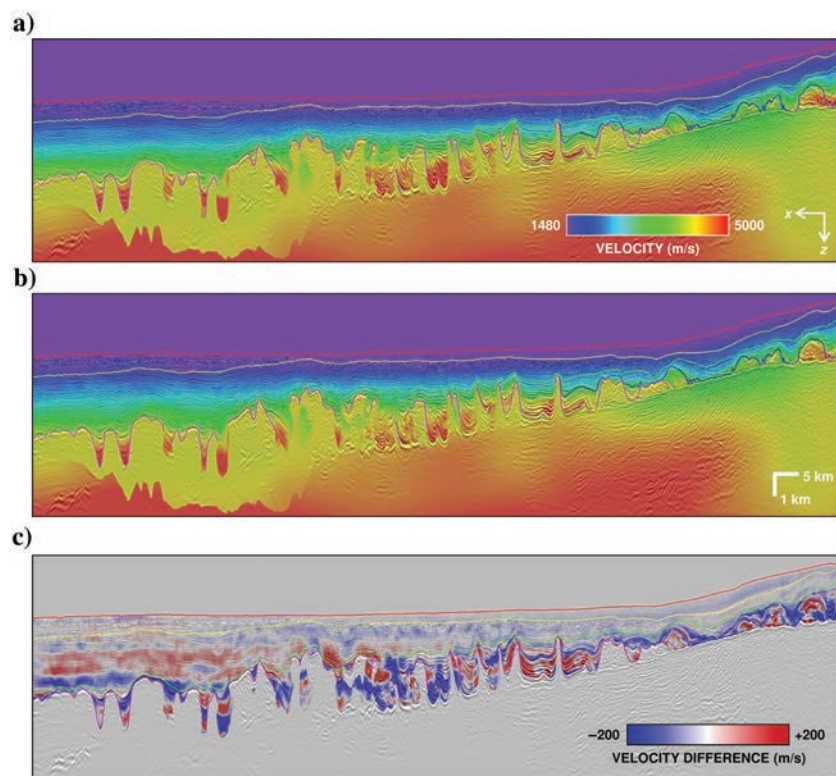


**Figure 6.** Inline section of the velocity model: (a) before the FWI update, (b) after the FWI update, and (c) the perturbation from FWI. The models are overlaid with an image migrated with the associated velocity model, and the salt has been inserted into both models post-FWI to aid the geologic context. Regional horizons are also shown to offer additional context, although the scale of the image means changes related to the FWI update are very hard to see. Hence, for the remaining images, we mainly focus on zoom displays of various areas.



quency in the data, then, together with error estimates in these quantities, computes an estimate of the probability of cycle skipping between real and modeled synthetic data. Figure 12 shows an example of this process, where we consider a subset of the shot gathers, namely one every 10 km and every 10th sail line. We generate a QC attribute value for each seismic trace in the shot gather and plot it in an aerial sense using the trace receiver  $x$  and  $y$ . Again, we have to zoom into a specific region to see the detail. As a rule of thumb, we choose the 5% probability level as a threshold for starting to be concerned by cycle skipping. The before and after FWI displays shown in Figure 12a and 12b, respectively, highlight that the starting model is, in general, not cycle skipped and that the vast majority of the cycle skipping is reduced, or entirely removed, after application of FWI. The odd pocket remains here and there, flagging areas to look at in more detail. The small regions of potential cycle skipping on the starting model are most often seen in the nearest offsets, rather than at the far. This is slightly surprising because, if this was true cycle skipping, then we would expect it to be flagged in multiple regions on the gather. Our interpretation is that this is due to remaining low-frequency noise in the seismic data that is biasing the QC in this region.

## Geologic interpretation

The formation of the South Gabon basin started in Early Cretaceous times with the opening of the South Atlantic rift. During this time, the deposited fluvial and lacustrine type continental sediments now form today's primary hydrocarbon source and reservoirs rocks — these are the main targets at depths of more than 4000 m in the survey area. In later Aptian times, arid climate conditions prevailed with high evaporation rates and a salt layer was deposited as sea waters progressively made their way through the area. Figure 2 shows that, following a period of halokinesis, this salt is now heavily deformed. However, it still forms a major top seal across the basin, stopping and trapping hydrocarbons below in the Aptian reservoir sands. On a basin scale, helped by the ocean-ward tilt of the West Africa margin, the sediments overlying the salt slid downslope, with the salt acting like a regional detachment layer to aid the sliding process. This gave rise to the formation of a large-scale gravitational gliding complex over tens of thousands of square kilometers and resulted in very complex salt structures with many diapirs, thrusts, and canopies forming in the section. Other sources of complexity are the remaining pieces of the broken-up Albian carbonate shelf that are now sliding on the salt.

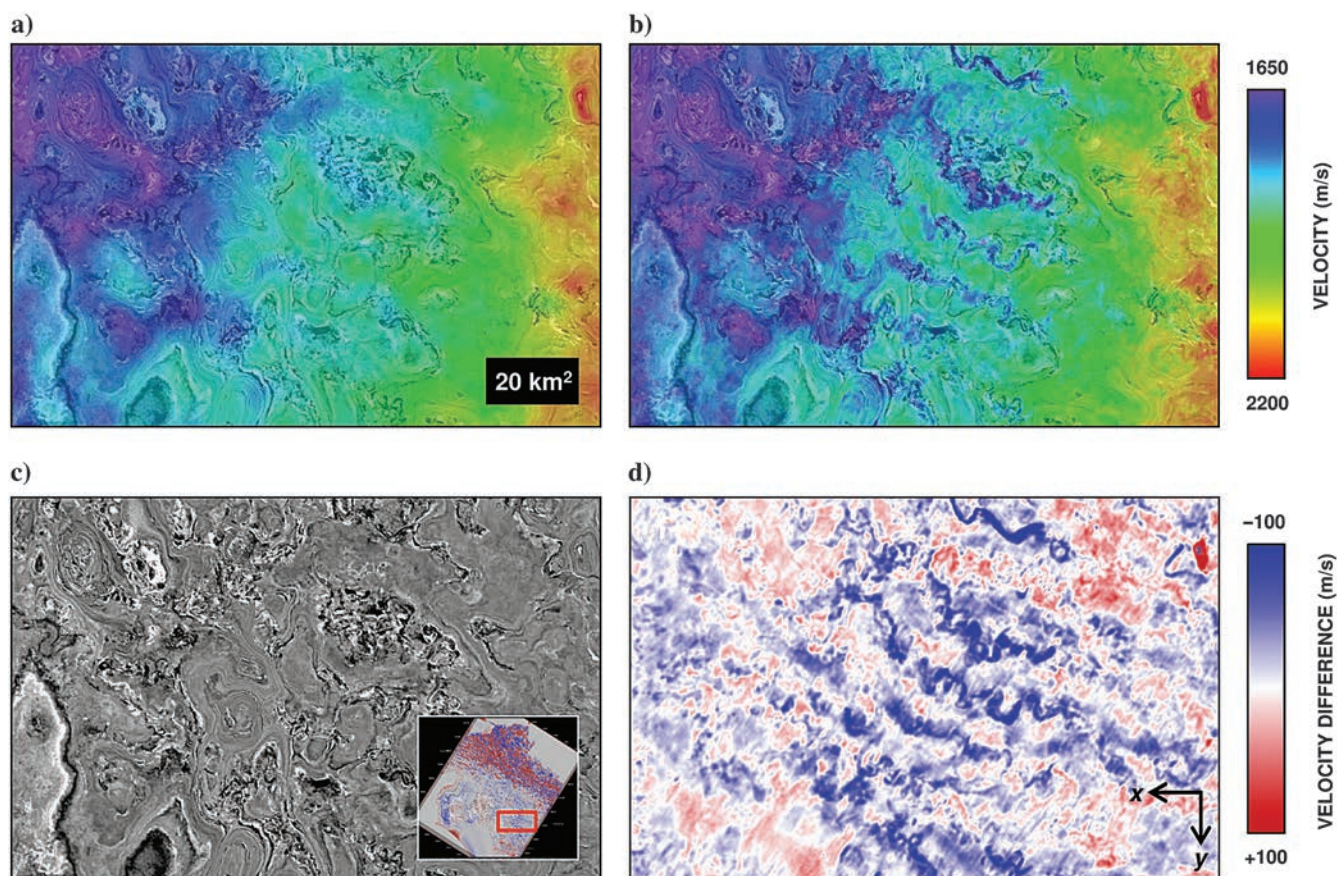


**Figure 7.** Depth slices at 3500 m for: (a) starting velocity model, (b) FWI velocity model, (c) seismic image migrated with FWI-velocity model, and (d) the velocity perturbation. The inset in (c) shows the approximately 1000 km<sup>2</sup> displayed area relative to the full area of the survey.



These so-called carbonate rafts generate prominent velocity anomalies in the seismic data. Figure 2 also shows that, in the southwesterly, downslope region on the left side of the display, we see a compressional domain characterized by tilted diapirs, complex extruded salt structures, thrust faulting, and folds. The transitional domain in the center of the display contains slightly simpler straight-up diapirs and local welds, whereas the northeasterly, upslope, extensional domain on the right

side is characterized by thin salt and pillows, carbonate rafts, normal faulting, and rollover anticlines.

All of these geologic aspects make velocity model building and seismic imaging very challenging, especially in the subsalt. In particular, we observe a correlation of poor presalt seismic data quality in the regions directly below the compressional salt structures, but see that the good presalt data quality returns when further to the southwest beyond the compressional

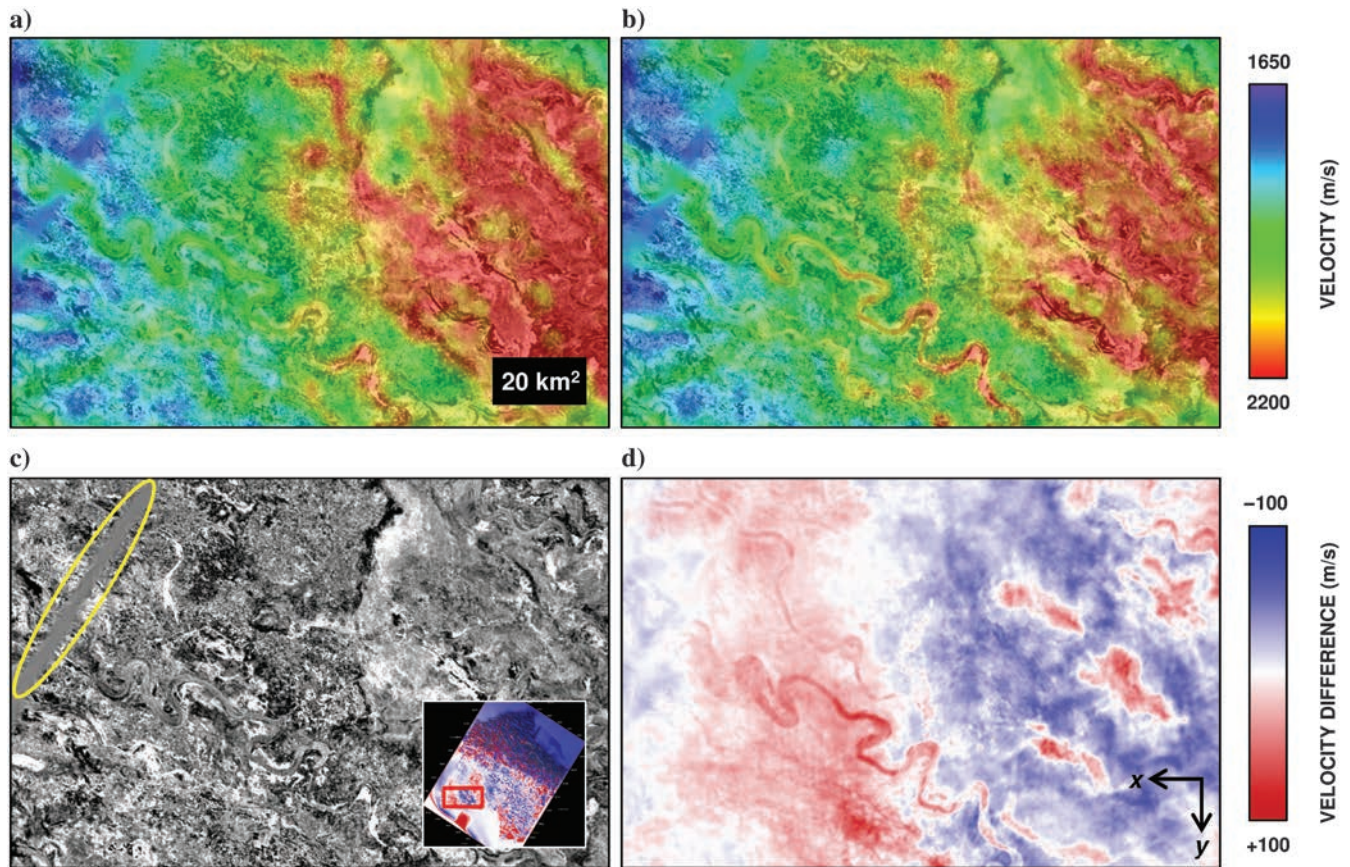


**Figure 8.** Depth slices at 3700 m for: (a) starting velocity model, (b) FWI velocity model, (c) seismic image migrated with FWI velocity model, and (d) the velocity perturbation. The inset in (c) shows the approximately 1000 km<sup>2</sup> displayed area relative to the full area of the survey. For reference, the oval yellow shape in (c) is a missing sail line that will be in-filled later.

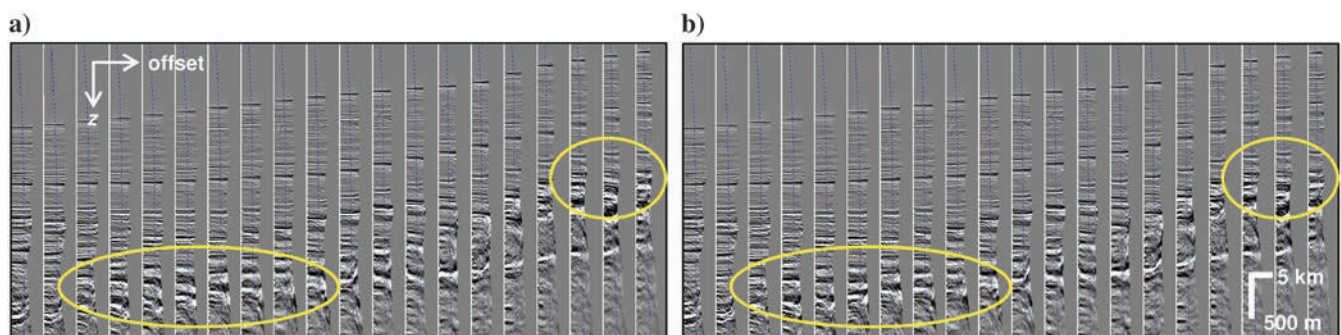


**Figure 9.** Comparison of common image gathers for a typical area in the survey: (a) before and (b) after the FWI update. In general, the gather flatness is improved by the FWI process, as indicated in the oval yellow regions. For reference, the gathers are displayed with a 50° incidence angle mute applied and a 30° incidence angle mute overlaid as the thin dotted blue line.



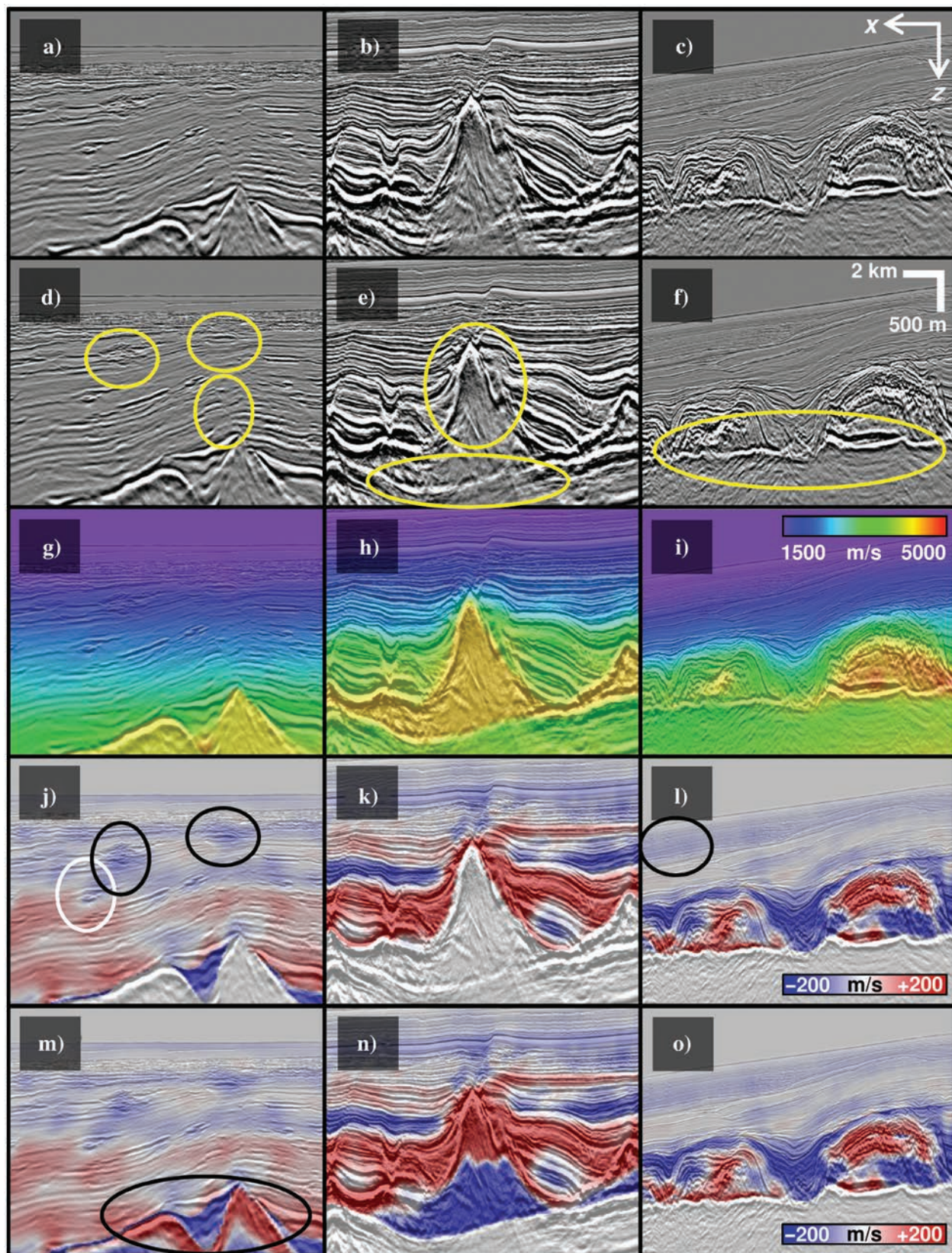


**Figure 10.** Examples from throughout the survey of the imaging: (a-c) before and (d-f) after the FWI update. The updated velocity model with the additional post-FWI salt flood is shown as an overlay in (g-i). Panels (j-l) and (m-o) show the raw FWI perturbation (before salt flood) with and without the top salt mute, respectively.



domain (not shown for reasons of space). Looking again at Figure 10, this shows zoomed-in displays from throughout the survey of the migrated seismic before and after the FWI update, for an example of each of these three domains: compressional in the left column, transitional in the middle column, and extensional in the right column. In one row on this figure, we also plot the FWI velocity model overlaid with the migrated section, as well as the perturbation with and without the top-salt mute, to highlight these features on the velocity model, thus aiding and reinforcing the interpretation. For example, Figure 10i shows that the FWI model

nically delineated the carbonate rafts, which have a faster velocity than the salt bodies here, with a slow-fast-slow internal structure. At the base salt level, prior to the FWI update, we see velocity pull-ups where the carbonate rafts are present and push-downs where they are absent and replaced by salt pillows. Comparing the displays in Figure 10c and 10f, we see that these distortions are improved when migrating with the FWI velocity model (recall that the FWI update did not significantly penetrate into the salt itself and that part of the model is subsequently replaced with a salt flood in these migrations). Also, we see that the location of the top-salt reflectors, and associated sharp velocity increase, are generally well-captured by FWI (see, e.g., the salt diapirs on the unmuted FWI perturbation in Figure 10m), although we note that we ended up muting this out and flooding for the reasons discussed earlier. Figure 10g and 10j highlights (white oval) where one of the sand channels above the salt/carbonate region is visible with a lower velocity than the surrounding sediments (the type of features seen in the depth slices of Figures 7 and 8). These types of channel features are very visible in the FWI velocity model and prevalent throughout the survey. If we now turn our attention to the shallower part of the section in Figure 10d and 10g, the first few 100 m of the near-surface Pliocene-Pleistocene section are known to be affected by polygonal faulting. This is indicative that these sediments are very unconsolidated and actively dewatering at present. This means they still contain large volumes of water, giving rise to a very low interval velocity (close to water velocity) that is visible in the very shallow part of the velocity display in Figure 10g. In this part of the section, we also see evidence for gas escape conduits in the seismic image and FWI velocity model (indicated in Figure 10l). Additionally, we are able to identify shallow bright amplitude packets (Figure 10d) as slow velocity gas pockets in the velocity model (Figure 10j, black ovals). These sharp, localized, low-velocity “bubbles”

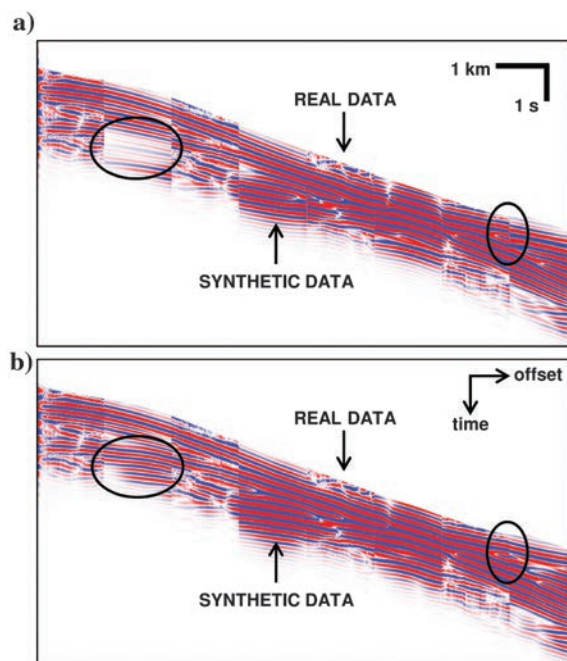


**Figure 11.** The QC of interleaved blocks of real and modeled synthetic data filtered to 4 Hz: (a) before and (b) after the FWI update.

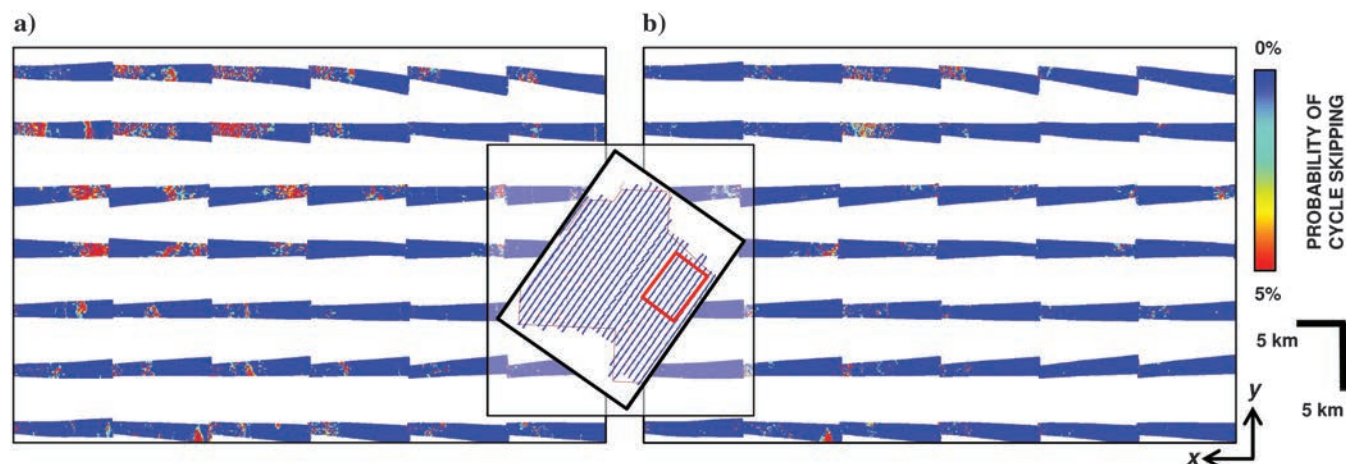


**Figure 12.** The QC showing the probability of cycle-skipping attribute evaluated at 4 Hz: (a) before and (b) after the FWI update. This display shows data for a shot pattern every 10 km along the sail line and every 10th sail line. This display can be repeated for the different frequency bands as the inversion proceeds.



are typically associated with high absorption in the seismic data and give rise to a push-down effect on the image due to the anomalous velocity. The low velocity detected by FWI allows the subsequent image to improve below these anomalies, as seen when comparing Figure 10a and 10d. In terms of the location of these anomalies, they are typically seen directly above the crest of the salt diapirs and capped by a gas-hydrate-related bottom-simulating reflector. This bottom-simulating reflector can generate a strong reflector in the near surface, and it is the phase-transition zone in the gas hydrates from frozen to unfrozen as the temperature increases with depth. All of these are interpretation elements that might be of interest in a shallow hazard drilling plan, the seismic imaging of which has been improved by using FWI.

### Suggestions for further study

This work forms part of a larger project on two levels: first, as part of an imaging and velocity-model build of the whole area down to basement level and, second, as part of a larger integrated geology and geophysics study of this region. In this paper, the former aspect is more relevant and we focus our discussion about potential future work on the imaging and velocity-model build.

An FWI update of [Thomsen's \(1986\)](#) epsilon parameter has shown to give further uplift in the imaging in various test swaths, as well as highlighting interesting geologic anomalies in the anisotropy parameter itself, and is being run on the full production volume at the time of writing. Pushing FWI to a higher frequency should give more resolution in the shallower part of the model and could be a potential next step after the epsilon update. Also, a post-FWI tomography update in the salt and presalt levels is planned in the areas where the diving waves used to drive the FWI update did not penetrate, rather than the simple salt flood process used here. This should be beneficial to ensure flatter gathers and a better image at these depths. This uplift would be in addition to the already seen imaging improvements that have come from solving the velocity complexity in the postsalt region. As mentioned earlier, FWI is being used here within the larger velocity model-building process, rather than as a final, post-tomography, update to the velocity model after tomography has built the best possible model. Hence, running another pass of FWI post-tomography might be beneficial to obtain further improvement in the top-salt area (with reference to the iterative workflow discussed earlier in the section "FWI methodology"). Also, at this stage, having a more open mute on the shot gathers, to allow reflection energy into the update, would add detail in the velocity model at depths beyond the diving wave penetration. These are potentially useful, although we note the previously discussed caveats related to the fact that these deep FWI updates will be reflection driven and their validity assumes tomography has already been able to accurately estimate the macromodel at this

depth. In terms of the imaging, all of the displays shown here are generated from a controlled beam migration for a QC of the FWI process only — this will not be the final imaging product of the project. The final migration will be done by a reverse time migration process that is well known to provide improved imaging in complex velocity models, such as the one we have presented. Finally, we would like to mention another interpretational aspect that is yet to be investigated but is potentially very interesting, namely the use of the FWI velocity model in a pore-pressure prediction study.

### Conclusion

In this paper, we have presented results for an extremely large case study from offshore Gabon showing a velocity model built using FWI and the subsequent imaging uplift and geologic interpretation. We have put to the test the general acknowledgement that FWI can work well on field data sets in areas probed by diving waves by processing a very large volume (approximately 25,000 km<sup>2</sup>) and find that it performs well. The implications of this work are to show the size of data volumes that can now be processed with FWI, as well as offering the exciting prospect of having a high-resolution velocity model to provide additional context and insight into the geology of the region. In return, such geologic interpretation serves as a feedback loop to control the quality of the FWI results.

### Acknowledgments

We gratefully acknowledge CGG and the Direction Générale des Hydrocarbures (DGH) of Gabon in the publication of this work and CGG's Multi-Client & New Ventures business line for their kind permission to show the Gabon data set. We would also like to thank our colleagues in CGG for their support, especially P. Gabrielli, R. Schouten, B. Gosling, and the rest of the Gabon processing project team, as well as S. Thompson for his additional geologic and interpretation input and G. Conroy for his assistance with the production FWI work. Finally, we gratefully acknowledge the contributions of associate editor D. Vigh, reviewer J. Hobro, and two other anonymous reviewers for their help in improving the final quality of this paper.

### References

- Bunks, C., F. M. Saleck, S. Zaleski, and G. Chavent, 1995, Multiscale seismic waveform inversion: *Geophysics*, **60**, 1457–1473, doi: [10.1190/1.1443880](https://doi.org/10.1190/1.1443880).
- Chauris, H., and R.-E. Plessix, 2013, Differential waveform inversion – A way to cope with multiples?: 75th Annual International Conference and Exhibition, EAGE, Extended Abstracts, Workshop paper, F06.
- Davison, C. M., and G. Poole, 2015, Far-field source signature reconstruction using direct arrival data: 77th Annual International Conference and Exhibition, EAGE, Extended Abstracts, Th N116 15.

- Duval, G., and J. Firth, 2015, G&G integration enhances acquisition of multi-client studies offshore Gabon: *World Oil*, **July**, 57–61.
- Gardner, G. H. F., L. W. Gardner, and A. R. Gregory, 1974, Formation velocity and density—The diagnostic basics for stratigraphic traps: *Geophysics*, **39**, 770–780, doi: [10.1190/1.1440465](https://doi.org/10.1190/1.1440465).
- Guillaume, P., G. Lambaré, O. Leblanc, P. Mitouard, J. Le Moigne, J.-P. Montel, T. Prescott, R. Siliqi, N. Vidal, X. Zhang, and S. Zimine, 2008, Kinematic invariants: An efficient and flexible approach for velocity model building: 78th Annual International Meeting, SEG, Expanded Abstracts, 3687–3692.
- Jones, C. E., M. Evans, A. Ratcliffe, G. Conroy, R. Jupp, J. I. Selvage, and L. Ramsey, 2013, Full waveform inversion in a complex geological setting: A narrow azimuth towed streamer case study from the Barents sea: 75th Annual International Conference and Exhibition, EAGE, Extended Abstracts, We 11 06.
- Jupp, R., A. Ratcliffe, and R. Wombell, 2012, Application of full waveform inversion to variable-depth streamer data: 82nd Annual International Meeting, SEG, Expanded Abstracts, doi: [10.1190/segam2012-0613.1](https://doi.org/10.1190/segam2012-0613.1).
- Kumar, R., B. Bai, and Y. Huang, 2014, Using reflection data for full waveform inversion: A case study from Santos Basin, Brazil: 76th Annual International Conference and Exhibition, EAGE, Extended Abstracts, Th E106 15.
- Lailly, P., 1983, The seismic inverse problem as a sequence of before stack migrations: Proceedings of the International Conference on Inverse Scattering, Theory, and Applications: SIAM.
- Martinez-Sansigre, A., and A. Ratcliffe, 2014, A probabilistic QC for cycle-skipping in full waveform inversion: 84th Annual International Meeting, SEG, Expanded Abstracts, 1105–1109.
- Ni, Y., T. Payen, and A. Vesin, 2014, Joint inversion of near-field and far-field hydrophone data for source signature estimation: 84th Annual International Meeting, SEG, Expanded Abstracts, 57–61.
- Plessix, R.-E., 2006, A review of the adjoint-state method for computing the gradient of a functional with geophysical applications: *Geophysical Journal International*, **167**, 495–503, doi: [10.1111/j.1365-246X.2006.02978.x](https://doi.org/10.1111/j.1365-246X.2006.02978.x).
- Plessix, R.-E., 2009, Three-dimensional frequency-domain full-waveform inversion with an iterative solver: *Geophysics*, **74**, no. 6, WCC149–WCC157, doi: [10.1190/1.3211198](https://doi.org/10.1190/1.3211198).
- Pratt, R. G., 1999, Seismic waveform inversion in the frequency domain. Part 1: Theory and verification in a physical scale model: *Geophysics*, **64**, 888–901, doi: [10.1190/1.1444597](https://doi.org/10.1190/1.1444597).
- Ratcliffe, A., A. Karagul, C. Henstock, G. Conroy, and V. Vinje, 2013, QC of full waveform inversion: 75th Annual International Conference and Exhibition, EAGE, Extended Abstracts, Workshop paper, A03.
- Ratcliffe, A., A. Privitera, G. Conroy, V. Vinje, A. Bertrand, and B. Lyngnes, 2014, Enhanced imaging with high-resolution full-waveform inversion and reverse time migration: A North Sea OBC case study: *The Leading Edge*, **33**, 986–992, doi: [10.1190/tle33090986.1](https://doi.org/10.1190/tle33090986.1).
- Ratcliffe, A., C. Win, V. Vinje, G. Conroy, M. Warner, A. Umpleby, I. Stekl, T. Nangoo, and A. Bertrand, 2011, Full waveform inversion: A North Sea OBC case study: 81st Annual International Meeting, SEG, Expanded Abstracts, 2384–2388.
- Rickett, J., 2013, The variable projection method for waveform inversion with an unknown source function: *Geophysical Prospecting*, **61**, 874–881, doi: [10.1111/1365-2478.12008](https://doi.org/10.1111/1365-2478.12008).
- Sheriff, R. E., and L. P. Geldart, 1995, *Exploration seismology*: 2nd ed.: Cambridge University Press.
- Sirgue, L., O. I. Barkved, J. P. van Gestel, O. J. Askim, and J. H. Kommendal, 2009, 3D waveform inversion in Valhall wide-azimuth OBC: 71st Annual International Conference and Exhibition, EAGE, Extended Abstracts, U038.
- Soubaras, R., 2010, Deghosting by joint deconvolution of a migration and a mirror migration: 80th Annual International Meeting, SEG, Expanded Abstracts, 3406–3410.
- Soubaras, R., and R. Dowle, 2010, Variable-depth streamer – A broadband marine solution: *First Break*, **28**, 89–96.
- Sun, D., and W. W. Symes, 2012, Waveform inversion via nonlinear differential semblance optimization: 82nd Annual International Meeting, SEG, Expanded Abstracts, doi: [10.1190/segam2012-1190.1](https://doi.org/10.1190/segam2012-1190.1).
- Tarantola, A., 1984, Inversion of seismic reflection data in the acoustic approximation: *Geophysics*, **49**, 1259–1266, doi: [10.1190/1.1441754](https://doi.org/10.1190/1.1441754).
- Thomsen, L. A., 1986, Weak elastic anisotropy: *Geophysics*, **51**, 1954–1966, doi: [10.1190/1.1442051](https://doi.org/10.1190/1.1442051).
- Vinje, V., G. Roberts, and R. Taylor, 2008, Controlled beam migration: A versatile structural imaging tool: *First Break*, **26**, 109–113.
- Virieux, J., and S. Operto, 2009, An overview of full-waveform inversion in exploration geophysics: *Geophysics*, **74**, no. 6, WCC1–WCC26, doi: [10.1190/1.3238367](https://doi.org/10.1190/1.3238367).
- Wang, K., B. Deng, Z. Zhang, L. Hu, and Y. Huang, 2015, Top of salt impact on full waveform inversion sediment velocity update: 85th Annual International Meeting, SEG, Expanded Abstracts, 1072–1077.
- Wang, Y., X. Chang, and H. Hu, 2014a, Simultaneous reverse time migration of primaries and free-surface related multiples without multiple prediction: *Geophysics*, **79**, no. 1, S1–S9, doi: [10.1190/geo2012-0450.1](https://doi.org/10.1190/geo2012-0450.1).
- Wang, Y., Y. Zheng, X. Chang, and Z. Yao, 2014b, Full waveform inversion using free-surface related multiples as natural blended sources: 76th Annual International Conference and Exhibition, EAGE, Extended Abstracts, We 106 16.
- Warner, M., A. Ratcliffe, T. Nangoo, J. Morgan, A. Umpleby, N. Shah, V. Vinje, I. Stekl, L. Guasch, C. Win, G. Conroy, and A. Bertrand, 2013, Anisotropic 3D full-waveform inversion: *Geophysics*, **78**, no. 2, R59–R80, doi: [10.1190/geo2012-0338.1](https://doi.org/10.1190/geo2012-0338.1).



Zhang, Y., H. Zhang, and G. Zhang, 2011, A stable TTI reverse time migration and its implementation: *Geophysics*, **76**, no. 3, WA3–WA11, doi: [10.1190/1.3554411](https://doi.org/10.1190/1.3554411).

Ziolkowski, A., G. E. Parkes, L. Hatton, and T. Haughland, 1982, The signature of an air gun array: Computation from near-field measurements including interactions: *Geophysics*, **47**, 1413–1421, doi: [10.1190/1.1441289](https://doi.org/10.1190/1.1441289).



**Bingmu Xiao** received a B.A. (2011) in applied geophysics from Jilin University, China, and an M.S. (2013) in geophysics from King Abdullah University of Science and Technology. She joined CGG in 2014 as a geophysicist in UK subsurface imaging. During her time at CGG, she has worked on a number of FWI projects from offshore

West Africa and the North Sea.



**Nadezhda Kotova** received an M.S. with honors in physics from the Moscow Engineering Physics Institute and a Ph.D. in physics from Heriot-Watt University. In 2012, she joined CGG as a geophysicist working in UK subsurface imaging. In her time at CGG, she has worked on a number of depth velocity model-building projects that

implemented FWI.



**Samuel Bretherton** received a B.Sc. and an M.S. in mathematics from the University of Bristol and the University of Sussex, respectively, prior to joining CGG in 2013. Since then, he has worked as a geophysicist in the UK subsurface imaging department, where he has been involved in a number of depth velocity model builds, including FWI in a variety of projects.



**Andrew Ratcliffe** received a B.Sc. in mathematics and physics and a Ph.D. in astrophysics from the University of Durham, UK, and joined the oil industry in 1996. He has worked in various seismic processing research and development roles for CGG, Veritas DGC, CGGVeritas, and now CGG again, all in the UK. His geophysical

research interests over the years have included amplitude variation with offset, automatic velocity picking, signal processing, and land processing. In recent times, he has been active in the area of FWI within CGG's UK-based research team, where he leads a research group specializing in this topic. His work in this area, titled "Anisotropic 3D full-waveform inversion," won the Best Paper in *GEOPHYSICS* award for 2013, coauthored with Imperial College, London, and ConocoPhillips Norge.



**Gregor Duval** received an M.S. in geology from the National School of Geology of Nancy in France and an M.S. in geophysics from the Earth Sciences University of Strasbourg. He is the senior technical manager for the geoscience team within the Multi-Client and New Ventures business line of CGG. He has worked for CGG for

more than 10 years, during which he has had various technical roles in seismic interpretation. He has led the multient client integrated geoscience team since 2011. His experience covers mainly the North Sea basins, Atlantic margin basins, West Africa, the Mediterranean Sea, the Caspian Sea, and the Banda Arc basins in Indonesia.



**Chris Page** received a B.Sc. (2002) in geophysics from Lancaster University, UK. He started his career as a geophysicist for Veritas DGC and has worked in various roles in seismic imaging for CGG. He currently leads a group of imaging teams working on a diverse portfolio of projects including multicomponent, time-lapse, depth imaging, and velocity-model building.



**Owen Pape** received a B.Sc. (2006) in geophysics with honors from the University of Edinburgh. He then joined Veritas DGC, now CGG, as a geophysicist working in UK subsurface imaging. His research interests include depth imaging and velocity model building, which includes FWI, where he supervises a number of seismic processing

teams.